





## Dynamic compression of soft layered materials yields tunable and spatiotemporally evolving surface patterns

Brianna MacNider,<sup>1</sup> Xudong Liang <sup>1</sup>, Samantha Hoang,<sup>2</sup> Maroun Abi Ghanem <sup>3</sup>,  
Shengqiang Cai <sup>1</sup> and Nicholas Boechler<sup>1,\*</sup>

<sup>1</sup>*Department of Mechanical and Aerospace Engineering, University of California San Diego, 9500 Gilman Drive, La Jolla, California 92093, USA*

<sup>2</sup>*Department of Mechanical Engineering, Seattle University, 901 12th Ave, Seattle, Washington 98122, USA*

<sup>3</sup>*Université Claude Bernard Lyon 1, CNRS, Institut Lumière Matière, F-69622 Villeurbanne, France*

 (Received 26 October 2021; revised 21 September 2022; accepted 17 February 2023; published 17 March 2023)

Soft layered systems buckling to form surface patterns has been widely studied under quasistatic loading. Here, we study the dynamic formation of wrinkles in a stiff-film-on-viscoelastic-substrate system as a function of impact velocity. We observe a spatiotemporally varying range of wavelengths, which display impactor velocity dependence and exceed the range exhibited under quasistatic loading. Simulations suggest the importance of both inertial and viscoelastic effects. Film damage is also examined, and we find that it can tailor dynamic buckling behavior. We expect our work to have applications to soft elastoelectronic and optic systems and open routes for nanofabrication.

DOI: [10.1103/PhysRevE.107.035002](https://doi.org/10.1103/PhysRevE.107.035002)

Mechanical surface instabilities are commonly observed in soft, solid systems containing interfaces [1] and can lead to the formation of periodic surface morphologies, including wrinkles [2–5], ridges [6,7], and folds [8]. Such surface instabilities both are widely observed in nature [9–11] and have been proposed for use in a variety of applications, ranging from material property metrology [12,13] to flexible electronics [14–16] and nanofabrication [17]. A canonical setting for exploring such mechanics has been stiff films layered on a softer substrate [18] (including studies where the substrate is liquid [19,20]). For the stiff-film-on-soft-substrate system, the surface patterns start as a single-wavelength sinusoid, then follow a known path within increasing strain, dictated by the material properties, layer thickness, and boundary conditions, which results in period doubling, period quadrupling, or transitions into periodic arrays of folds [8] (such modes have not been shown for films on liquids).

Studies exploring the dynamic response of stiff-film-on-soft-substrate systems have introduced further complexity and shown that dynamic loading can lead to progressive formation, and evolving wavelengths, of the sinusoidal surface wrinkling patterns [21–23]. Analogies to this complexity introduced by dynamic loading can also be seen by contrasting quasistatic and dynamic buckling of thin bars [24,25], filaments [26], smectic bubbles [27], and films [21,28] in fluids, albeit their taxonomy is less diverse than that of stiff films on soft substrates.

In this paper, we demonstrate how high-amplitude dynamic loading of stiff-film-on-soft-substrate systems yields hitherto unreported surface patterns. As in Ref. [22], our system consists of a polydimethylsiloxane (PDMS) block bonded to a

stiffer film (herein we use a Kapton film, whereas the prior study used a softer, PDMS film). The system is impacted with a striker plate, resulting in the propagation of a bulk wave and initiation of wrinkling patterns on the surface (shown in Fig. 1). The response was captured via high-speed video, analyzed via digital image processing, and then modeled using finite element method (FEM) simulations. In both experiment and simulation, we observe the dynamic formation of surface patterns containing numerous, non-integer-multiple wavelengths that evolve across both space and time, are tunable with striker velocity, and are shorter than those exhibited under quasistatic loading. We also study how the presence of even small amounts of deviation from a flat film profile, such as may be caused by prior testing or intentionally designed into the system [29–31], has a drastic effect on the subsequent dynamic surface morphology evolution.

The PDMS blocks used are of length  $L = 50.4$  mm, have a square cross section of side length  $w = 37$  mm, and are bonded on one side to a stiffer Kapton tape film with a thickness of  $t = 102$   $\mu\text{m}$ . Six nominally identical samples [32] were fabricated to perform tests at varying impact velocities without contaminating the results with potential damage induced by prior impacts. To confirm comparability between samples, quasistatic compression tests were performed on each sample. Quasistatic testing past the point of period doubling was only conducted on sample 1 [the sample impacted at 1.9 m/s; see Figs. 1(a) and 1(c)]. Each sample was subsequently tested by impacting them in their “pristine” state (not previously exposed to dynamic loading) at speeds varying from 1.9 to 8.9 m/s. The striker compressed the samples about  $\delta L = 8.6 \pm 0.1$  mm before being halted by stoppers [Fig. 1(b)]. The impact sent a large-amplitude, low-frequency compression wave through each sample, which caused the film to form wrinkles. After imaging the sample at 30 kfps

\*Corresponding author: [nboechler@ucsd.edu](mailto:nboechler@ucsd.edu)

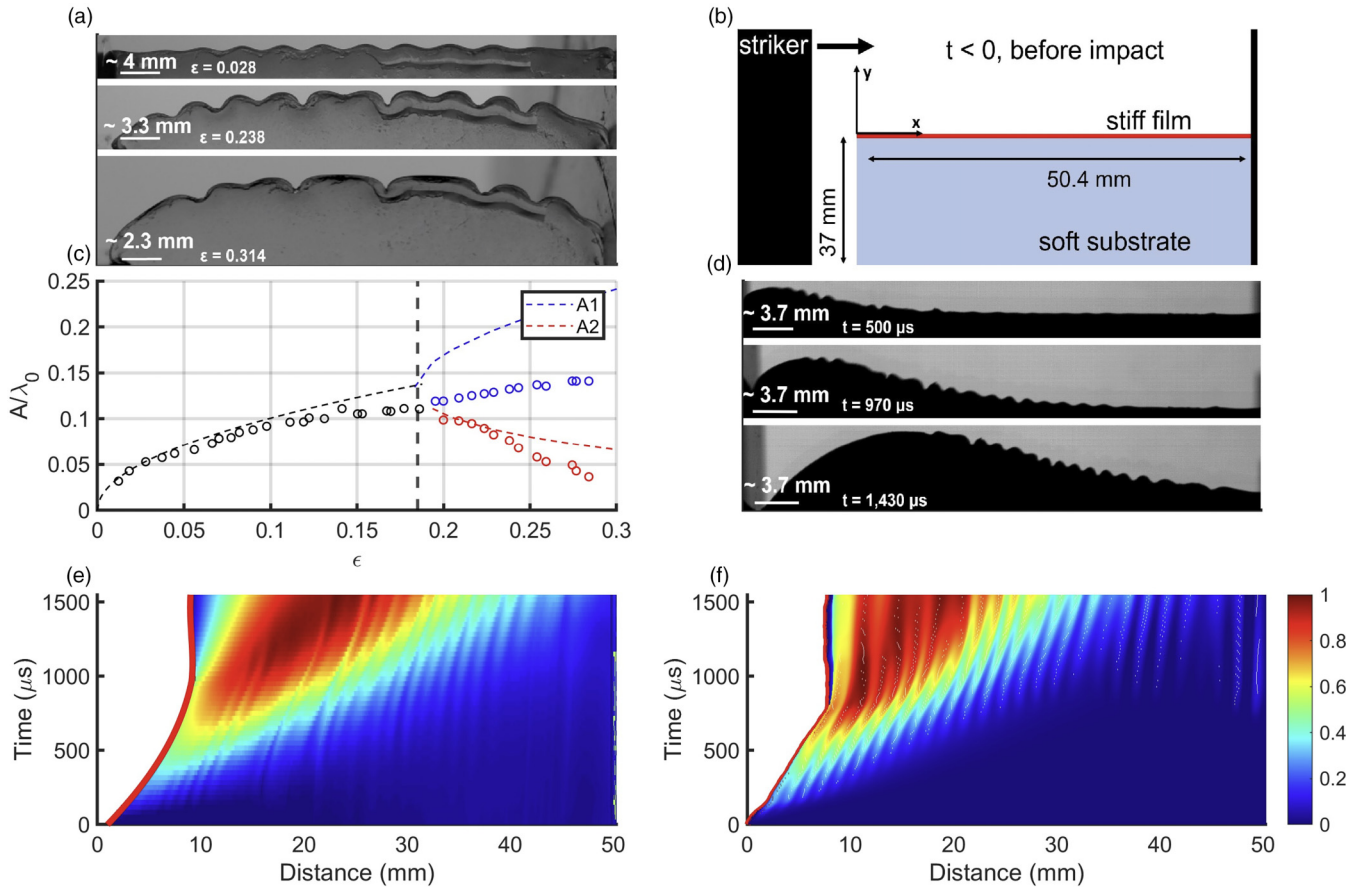


FIG. 1. (a) Pre-impact-test quasistatic compression of sample 1 yields period-doubling behavior. (b) The dynamic test setup. (c) Measured (open circles) and predicted (dashed curves) quasistatic wrinkle amplitude vs strain, corresponding to the test shown in (a). After the critical strain (vertical thick dashed line), the period-doubled mode (blue, top branch) grows, and the original mode (red, bottom branch) fades. (d) Snapshots from a test at 7.1 m/s impactor velocity on a “pristine” sample, displaying multiple-wavelength surface patterns. (e) A normalized spatiotemporal diagram of the experiment shown in (d), with color representing the  $y$ -direction surface displacement,  $U_y$ . The line visible at the right edge is an artifact of the camera frame edge and should be disregarded. (f) A normalized spatiotemporal diagram of the simulation [7.6 m/s impact velocity, same color scheme as in (e)].

(kfps refers to 1000 frames per second), an edge detection algorithm was used to track the surface profile for all images. The low-frequency portion of the displacement was subtracted to isolate the wrinkles for further analysis, and a spatial fast Fourier transform (FFT) was then performed at each time step.

The described image analysis procedure was used to obtain the wrinkling amplitude  $A$  as a function of quasistatic strain  $\epsilon$ . For convenience, we take  $\epsilon > 0$  as compression. The measured response in Fig. 1(c) (open circles) mirrors prior studies [8,33], where at a critical strain  $\epsilon_0$  the sample buckles to a mode of wavelength  $\lambda_0$ . For sample 1,  $\lambda_{0,1} = 4.1$  mm (where the second subscript denotes the sample number), whereas the initial buckling wavelength averaged across all samples was  $\lambda_{0,av} = 3.8$  mm (standard deviation of 0.24 mm). Sample 1 exhibits period doubling to a wavelength of  $\lambda_{1,1}$  at strain  $\epsilon_1 = 0.185$ , and then eventual period quadrupling. The dashed curves in Fig. 1(c) denote predictions from the analytical model of Ref. [33], using the measured  $\lambda_{0,1}$ . We attribute the post-period-doubling deviations between the measurements and the model to reduced compression at the sample surface due to the sample curling around the edge of the compression plates.

Representative images from the impact experiments are shown in Fig. 1(d), which display shorter wavelengths than the quasistatic case [Fig. 1(a)], and the wrinkling wavelength appears to vary across time and the length of the sample. Using the same image analysis procedure for the quasistatic case, this variation is also observable in a spatiotemporal plot of the measured out-of-plane surface displacement [Fig. 1(e)]. These qualitative observations hold across all experiments performed, although the wavelengths present vary.

The impact tests were modeled via FEM simulations (Abaqus/CAE) [32]. A moving boundary matching impactor profile of the first (and slowest) dynamic experiment was applied, which was subsequently scaled up for higher-impact-velocity cases. In Fig. 1(f), we show the simulated spatiotemporal evolution of the out-of-plane surface displacement for a similar impact velocity to that used in the experiment of Figs. 1(d) and 1(e).

In Fig. 2, we show spatial FFT spectra of the quasistatic compression test [corresponding to the data in Figs. 1(a) and 1(c)] and simulated and experimental dynamic compression tests (2.5 and 1.9 m/s impactor velocities, respectively). In Fig. 2(a), the emergence of period-doubled and period-

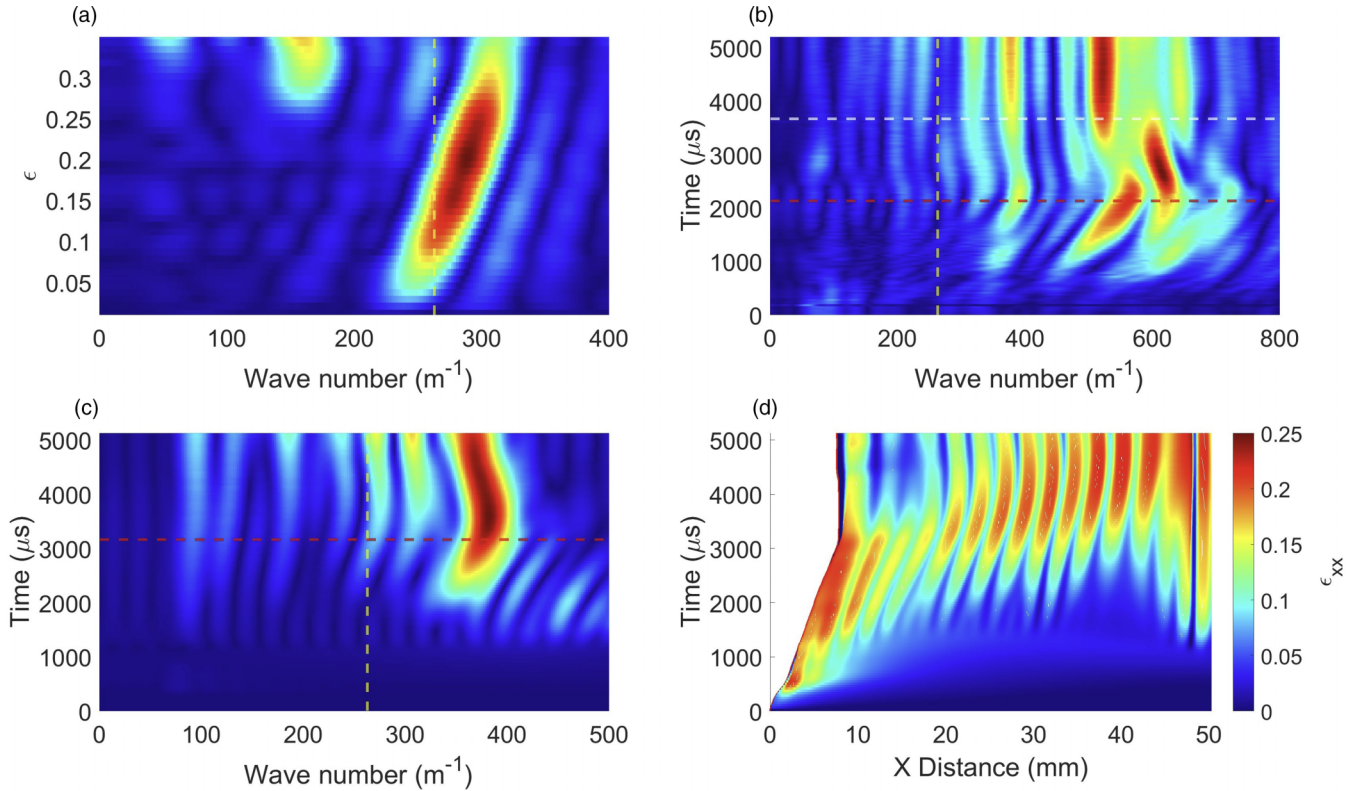


FIG. 2. (a) FFT of the sample 1 quasistatic compression test. FFT of a dynamic test (b) and FEM simulation (c), with impact speeds of 2.5 and 1.9 m/s, respectively. Wave number  $\sim 263 \text{ m}^{-1}$  corresponds to  $\lambda_{0,\text{av}}$  and is shown as the dashed vertical yellow lines in (a)–(c). The horizontal red dashed lines in (b) (lower horizontal dashed line) and (c) (sole horizontal dashed line) represent the time at which the striker hits the stop blocks and comes to a stop, while the white (upper) horizontal dashed line in (b) represents the time of arrival at the right edge of the peak of the bulk compression wave. This same bulk wave arrival time in (c) and (d) is the upper limit of the times shown. (d) Spatiotemporal evolution of strain obtained from the FEM simulation in (c), averaged over a depth of  $\lambda_{0,1}$  (compression shown as positive).

quadrupled modes with increasing applied quasistatic strain can be seen. In Figs. 2(b) and 2(c), corresponding to the impact experiment and simulation, respectively, a complex spatiotemporal evolution involving multiple wavelengths is observed, marking a stark, qualitative difference from the quasistatic response. The wave numbers (here, defined as  $1/\lambda$ ) emerging from the dynamic tests uniformly exceed the quasistatic wave numbers. The simulated local strain  $\epsilon$  (normal strain in the  $x$  direction, averaged over a depth of  $\lambda_{0,\text{av}}$  in the  $y$  direction) is shown in Fig. 2(d) to reach values higher than  $\epsilon_1$ . Thus, while the average sample strain is less than  $\epsilon_1$  in the cases of Figs. 2(b) and 2(c), localized period doubling might be expected. However, none of the observed modes was found to be an obvious factor of two multiples of the others. The sole exception to this is sample 1 [32], which displayed one dominant buckling wavelength, out of many, that approached the period-doubled mode wavelength. We suggest that this is because sample 1 was the sole case to be quasistatically tested past the period-doubling point prior to dynamic testing (this observation is later explored more fully).

The impact tests of Fig. 2 showed an upward wave-number shift from the quasistatic response. The range of wavelengths of the most prominent peaks emerging from the impact experiments are consistently two to four times smaller than  $\lambda_{0,\text{av}}$  ( $\sim 1\text{--}2 \text{ mm}$ ), even after the passage of the bulk compression wave when relaxation dominates. Quantifying the measured

spectra from experimental and simulated impact tests, we take the spectral centroid of each spectrum, for each time step, and examine the averages and maxima. We note that the maximum values consist of phenomena mainly driven by the compression regime, while the average values contain data from both the compression and relaxation regimes. The limits of the considered wave-number range for the spectral centroid analysis are set to 50% of the maximum amplitude in each case. Figure 3(a) shows a positive dependence of the maximum (compression-dominated regime) wave-number spectral centroid on velocity. We note a change in the observed striker velocity dependence in the experimental data at 5.6 m/s, which corresponds to the test at which the striker recoil first results in a complete detachment between the striker and sample. This detachment introduces a competing tension which reduces the strength of the compression regime. All simulations were run without this recoil in order to study the expected trend had recoil not been present, and a clear speed-dependent increase in wave number is observed [Fig. 3(b)]. We also note a drop in the wrinkle amplitude as impact velocity is increased, highlighted in Figure S9 in the Supplemental Material [32].

We suggest that the increase in observed wave number with increasing impact speed (and with respect to quasistatic loading) can, in part, be accounted for by the viscoelasticity of the substrate. We model our substrate as a standard linear solid

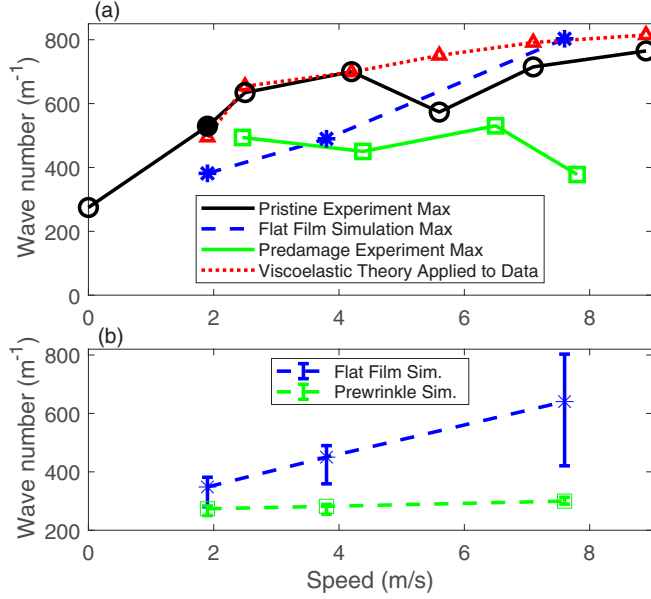


FIG. 3. (a) The maximum spectral centroid (in time) of the dynamically tested samples. Shown are results from pristine sample experiments (black circles), predamaged sample experiments (green squares), flat film simulations (blue stars), and substitution of measured  $\omega$  into Eq. (1) (red triangles). (b) Wave-number spectral centroids for flat film simulations (blue stars) and prewrinkle film simulations (green squares), with the average and the range between minimum and maximum values indicated by the error bars. Sim., simulation.

(SLS) material, where the magnitude of the dynamic elastic modulus can be described as [34]

$$E^* = \left| E_1 + E_0 \left( \frac{\omega^2 \tau_r^2}{1 + \omega^2 \tau_r^2} \right) + i E_0 \left( \frac{\omega \tau_r}{1 + \omega^2 \tau_r^2} \right) \right|. \quad (1)$$

$E_1 = 10$  MPa,  $E_0 = 130$  KPa,  $\tau_r = 90$   $\mu$ s, and the characteristic excitation frequency  $\omega$  is estimated by taking the temporal FFT of the striker position until rest (ignoring recoil), and identifying the frequency at half amplitude maximum. This approximation predicts a critical buckling wave number of 500–760 m<sup>-1</sup> [across all tests, shown in Fig. 3(a)], in good agreement with the measurements. Wavelength shift due to impact in systems containing viscous substrates has been noted in several other works. The authors of Ref. [24] examine an elastic filament in a viscous fluid compressed at various strain rates, and similarly find a decrease in buckling wavelength with increased strain rate. In Ref. [23], the effect of strain rate upon the compression of soft layered composites is studied, and viscoelastic stiffening is predicted to adjust the critical buckling wavelength with increased strain rate. In Ref. [21], a dynamic wavelength smaller than the quasistatic wavelength is observed, though wavelength dependence on impactor velocity is not present due to the domination of inertial over viscous effects.

Despite the described agreement, we suggest that viscoelasticity cannot be the sole contributing effect to the observed velocity dependence. Comparative simulations were conducted in which the viscoelastic behavior was removed from the substrate material properties (leaving a hyperelastic-

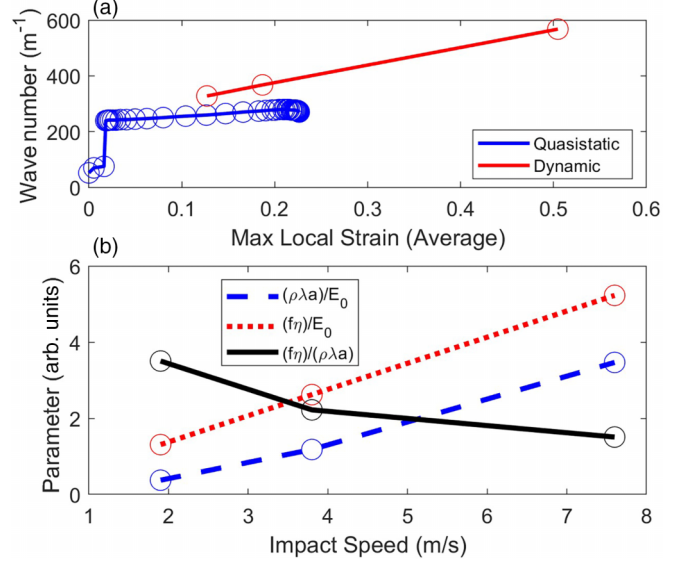


FIG. 4. (a) Wave-number maximum spectral centroid as a function of maximum local strain averaged over a depth of  $\lambda_{0,1}$  for purely hyperelastic substrate simulations, showing that even without viscoelasticity the combination of nonlinearity and inertial effects present in dynamic cases (red, upper line) can induce wave numbers significantly exceeding quasistatic compression (blue, lower line). (b) Dimensionless parameters estimating inertial ( $\rho\lambda a$ ), viscous ( $f\eta$ ), and elastic ( $E_0$ ) forces, where  $a$  is the maximum acceleration of the striker,  $\lambda$  is the wave-number maximum spectral centroid, and  $\rho$  is the material density, showing that as impact speed is increased, both inertial and viscous forces increase with respect to elastic forces, with inertial forces increasing at a faster rate than viscous ones.

only substrate model). A similar, though greatly reduced, downshift in wavelength was observed with increasing impact speeds [32]. Similarly, using the simulated response of the hyperelastic-only sample, we compare the maximum spectral centroid at similar strain levels between dynamic and quasistatic cases [Fig. 4(a)]. At comparable strain levels, hyperelastic-only simulations display a larger wave number in the dynamic case than in the quasistatic case, asserting that substrate nonlinearity alone cannot account for the observed wave-number shift (even in the absence of viscoelastic effects). This suggests a third contributing factor, which we posit may result from inertial effects. Using the simulated material properties and the characteristic excitation frequency, where  $f = \omega/(2\pi)$ , to estimate the relative magnitude of viscous, inertial, and elastic effects [Fig. 4(b)], we find that as impact velocity is increased, the importance of inertial effects increases relative to viscous and elastic effects (see Ref. [32] for more information).

In contrast to the wavelength velocity dependence, broadband wave-number content is not present in the aforementioned literature. Although wavelength is observed to evolve with time [21,23,24], it does not significantly vary spatially. A spatial wavelet analysis was performed on the experiments herein that confirms the presence of spatial wave-number variation at a given time [32]. We note that the nature of our experimental setup, in particular the presence of relaxation processes and bulk compression wave reflection, somewhat

complicates the examination of wavelength variation. References [26,27] noted wavelength variation as a function of global system contraction and expansion by observing the unchanging number of peaks across a given region. Separating out these regimes, therefore, is important in the effort to identify the presence and source of any spatial wavelength variation. We therefore take care to mark in all FFT analyses several times important to the separation of the pure compression and pure relaxation regimes, including the time at which the striker comes to a stop (and, in some cases, rebounds, inducing an earlier onset of the relaxation regime) and the time at which the peak of the bulk compression wave reaches the sample edge (after which reflection, and a relaxation-dominated regime, ensues). We consider phenomena occurring in the times before striker stop as being mainly compression driven, the times between striker stop and bulk wave rebound as being a mixture of compression and relaxation, and the times after bulk wave rebound as being relaxation dominated. Although pronounced wavelength variation is seen after the rebound of the bulk compression wave sends the entire sample into a relaxation regime, and we do note the expansion of wrinkles after passage of the bulk wave, significant variation in wavelength is present during early times in the region ahead of the bulk wave, when the initial striking of the sample drives a compression-dominated regime. In addition, we observe multiple distinct wavelengths which are not the result of a smooth transition between compressed and extended wrinkles of a single base wavelength. It is therefore unlikely that global and local length changes are the sole underlying cause of the spatial variation we see. Several other possible causes are considered. The strain rate herein varies from 38 to 180 s<sup>-1</sup>. This is much greater than the strain rates of Refs. [23,24], and although the maximum impact velocity in Ref. [21] is comparable to our lowest impact velocity, it is noted that inertia, rather than viscosity, dominates their system's response. We suggest the high impact velocity induces a spatial variation in viscoelastic stiffening, altering the effective localized elastic modulus, creating many localized " $\lambda_0$ " values. This could also enhance the nonlinear response of the system, by effectively dropping  $\epsilon_0$  [23]. This could also induce nonlinear interactions between spatially neighboring modes [35]. Such nonlinearity is absent, or much weaker, in systems with a fluid substrate (as in Ref. [21]).

Further evidence of viscoelasticity serving as the driving factor for spatial wave-number heterogeneity can be seen by comparing spatiotemporal variation of the wrinkling patterns, instantaneous dynamic modulus, and inertial forces found from simulations with combinations of elastic, hyperelastic, and viscoelastic properties [32]. Specifically, only in the cases with viscoelasticity are low-amplitude longitudinal waves racing ahead of the large-deformation bulk wave seen to alter, and induce a more complex spatial variation of, the instantaneous properties of the substrate before wrinkle formation. This is seen to result in a spatial wavelength heterogeneity in the case of the viscoelastic simulations during initial passage of the large-deformation bulk wave, which is not present in the elastic and hyperelastic cases [32].

Neither the wavelength decrease nor the spatial variation observed in this paper was observed in the prior, related study

of Ref. [22]. In this previous case, a single main wavelength was observed evolving across time, but with minimal spatial variation. As the substrates are nominally identical between the two studies, we look elsewhere for the cause of the discrepancy. It was noted in Ref. [22] that the sample studied therein was tested quasistatically and dynamically multiple times, while the samples in this paper were tested to low strain (excluding sample 1), quasistatically, a single time, and then dynamically only once to reach the prior results. Visual inspection of both current and previous samples after testing reveals small but observable indentations on the surface of the film [32], suggesting damage due to previous testing could be the cause of the observed differences. In order to explore the effect of predamage on the impact response, further experiments and simulations were performed. Simulations were run with an initial "prewrinkle" profile applied to the film. This prewrinkle profile was given a wavelength matching the expected quasistatic critical buckling wavelength, with amplitude set to a fraction of the thickness of the film. As observed in Ref. [22], a single prominent wavelength occurred near the quasistatic buckling wavelength, matching the prewrinkled pattern. Figure 3(b) shows the spectral centroid time average and range for both prewrinkled and flat film simulations, wherein the prewrinkled case shows a drastically reduced velocity dependence. Time averages were taken across the entirety of simulation run time, encompassing the full temporal evolution of the wave-number landscape. As flat film and prewrinkle simulations were run under the exact same conditions for each impact speed, with the only difference being the presence of film prewrinkling, time averages capture the same range of data between the flat film and prewrinkle cases, and the stark effect of the introduction of prewrinkling is clear. The examination of both the average and range of the spectral centroid highlights that this reduced velocity dependence holds across both compression (represented by the maximum centroid value) and relaxation (represented by the minimum centroid value) regimes. Retesting the previously-only-once-impacted samples, the maximum spectral centroid is shown in comparison to that of the pristine samples in Fig. 3(a), which reveals a lowered value of the maximum spectral centroid, as well as reduced velocity dependence. We note that a key difference between the "retested" samples herein and those of Ref. [22] is that the predamage was found to be aperiodic and periodic, respectively, thus giving different wave-number distributions but an otherwise similar qualitative response. In addition, we remind the reader that sample 1 was the only first-tested sample in this paper to display significant long-wavelength buckling prior to striker rebound. Given that sample 1 was the only sample tested past the quasistatic period-doubling point, it may contain weak predamage consistent with the first or second quasistatic buckling mode, and its wavelength content would therefore be expected to differ somewhat from the entirely "pristine" samples.

Through dynamic testing of stiff-film-on-soft substrate systems, we observe the emergence of spatiotemporally varying surface patterns. The system's velocity dependence, which we tie to viscous and inertial effects, may hold promise in the potential dynamic tuning of surface patterns in a system that classically can only be adjusted through change of its material properties. The complexity of the underlying causes

may provide motivation for improved nonlinear dynamical and viscous models capable of predicting the dynamic surface morphology evolution, which may further enable the informed design of new surface patterns as may be applicable to flexible electronics (e.g., nonlinear signal processing) and nanofabrication.

We thank John Hutchinson for insightful discussions. We acknowledge Guangcan Lu for early experiments exploring the impact response of PDMS blocks with Kapton tape surface films. This work was supported by the U.S. National Science Foundation (Grant No. CMMI-1536406) and the U.S. Army Research Office (Grant No. W911NF-20-2-0182).

- 
- [1] B. Li, Y.-P. Cao, X.-Q. Feng, and H. Gao, Mechanics of morphological instabilities and surface wrinkling in soft materials: a review, *Soft Matter* **8**, 5728 (2012).
- [2] Z. Huang, W. Hong, and Z. Suo, Nonlinear analyses of wrinkles in a film bonded to a compliant substrate, *J. Mech. Phys. Solids* **53**, 2101 (2005).
- [3] J. W. Hutchinson, The role of nonlinear substrate elasticity in the wrinkling of thin films, *Philos. Trans. R. Soc. A* **371**, 20120422 (2013).
- [4] S. Yang, K. Khare, and P.-C. Lin, Harnessing surface wrinkle patterns in soft matter, *Adv. Funct. Mater.* **20**, 2550 (2010).
- [5] N. Bowden, S. Brittain, A. G. Evans, J. W. Hutchinson, and G. M. Whitesides, Spontaneous formation of ordered structures in thin films of metals supported on an elastomeric polymer, *Nature (London)* **393**, 146 (1998).
- [6] Y. Cao and J. W. Hutchinson, Wrinkling phenomena in neo-Hookean film/substrate bilayers, *J. Appl. Mech.* **79**, 031019 (2012).
- [7] J. Zang, X. Zhao, Y. Cao, and J. W. Hutchinson, Localized ridge wrinkling of stiff films on compliant substrates, *J. Mech. Phys. Solids* **60**, 1265 (2012).
- [8] F. Brau, P. Damman, H. Diamant, and T. A. Witten, Wrinkle to fold transition: influence of the substrate response, *Soft Matter* **9**, 8177 (2013).
- [9] J. Yin, Z. Cao, C. Li, I. Sheinman, and X. Chen, Stress-driven buckling patterns in spheroidal core/shell structures, *Proc. Natl. Acad. Sci. USA* **105**, 19132 (2008).
- [10] A. Boudaoud, An introduction to the mechanics of morphogenesis for plant biologists, *Trends Plant Sci.* **15**, 353 (2010).
- [11] L. Wang, C. E. Castro, and M. C. Boyce, Growth strain-induced wrinkled membrane morphology of white blood cells, *Soft Matter* **7**, 11319 (2011).
- [12] J. Y. Chung, A. J. Nolte, and C. M. Stafford, Surface wrinkling: A versatile platform for measuring thin-film properties, *Adv. Mater.* **23**, 349 (2011).
- [13] A. Schweikart and A. Fery, Controlled wrinkling as a novel method for the fabrication of patterned surfaces, *Microchim. Acta* **165**, 249 (2009).
- [14] S. P. Lacour, S. Wagner, Z. Huang, and Z. Suo, Stretchable gold conductors on elastomeric substrates, *Appl. Phys. Lett.* **82**, 2404 (2003).
- [15] D. Kim and J. A. Rogers, Stretchable electronics: Materials strategies and devices, *Adv. Mater.* **20**, 4887 (2008).
- [16] D.-Y. Khang, J. A. Rogers, and H. H. Lee, Mechanical buckling: Mechanics, metrology, and stretchable electronics, *Adv. Funct. Mater.* **19**, 1526 (2009).
- [17] S. Singamaneni, M. E. McConney, and V. V. Tsukruk, Spontaneous self-folding in confined ultrathin polymer gels, *Adv. Mater.* **22**, 1263 (2010).
- [18] J. Genzer and J. Groenewold, Soft matter with hard skin: From skin wrinkles to templating and material characterization, *Soft Matter* **2**, 310 (2006).
- [19] R. Huang and Z. Suo, Wrinkling of a compressed elastic film on a viscous layer, *J. Appl. Phys.* **91**, 1135 (2002).
- [20] O. Kodio, I. M. Griffiths, and D. Vella, Lubricated wrinkles: Imposed constraints affect the dynamics of wrinkle coarsening, *Phys. Rev. Fluids* **2**, 014202 (2017).
- [21] F. Box, D. O’Kiely, O. Kodio, M. Inizan, A. A. Castrejón-Pita, and D. Vella, Dynamics of wrinkling in ultrathin elastic sheets, *Proc. Natl. Acad. Sci. USA* **116**, 20875 (2019).
- [22] M. Abi Ghanem, X. Liang, B. Lydon, L. Potocsnak, T. Wehr, M. Ghanem, S. Hoang, S. Cai, and N. Boechler, Wrinkles riding waves in soft layered materials, *Adv. Mater. Interfaces* **6**, 1801609 (2019).
- [23] V. Slesarenko and S. Rudykh, Harnessing viscoelasticity and instabilities for tuning wavy patterns in soft layered composites, *Soft Matter* **12**, 3677 (2016).
- [24] J. Chopin, M. Dasgupta, and A. Kudrolli, Dynamic Wrinkling and Strengthening of an Elastic Filament in a Viscous Fluid, *Phys. Rev. Lett.* **119**, 088001 (2017).
- [25] H. E. Lindberg, Impact buckling of a thin bar, *J. Appl. Mech.* **32**, 315 (1965).
- [26] S. M. Salili, T. Ostapenko, O. Kress, C. Bailey, W. Weissflog, K. Harth, A. Eremin, R. Stannarius, and A. Jákli, Rupture and recoil of bent-core liquid crystal filaments, *Soft Matter* **12**, 4725 (2016).
- [27] K. Harth, T. Trittel, K. May, and R. Stannarius, Dynamic wrinkling of freely floating smectic films, *Soft Matter* **15**, 6769 (2019).
- [28] L. Deike, J.-C. Bacri, and E. Falcon, Nonlinear waves on the surface of a fluid covered by an elastic sheet, *J. Fluid Mech.* **733**, 394 (2013).
- [29] C.-M. Chen, J. C. Reed, and S. Yang, Guided wrinkling in swollen, pre-patterned photoresist thin films with a crosslinking gradient, *Soft Matter* **9**, 11007 (2013).
- [30] E. Flores-Johnson, T. J. Rupert, K. J. Hemker, D. S. Gianola, and Y. Gan, Modelling wrinkling interactions produced by patterned defects in metal thin films, *Extreme Mech. Lett.* **4**, 175 (2015).
- [31] J.-H. Lee, H. W. Ro, R. Huang, P. Lemailet, T. A. Germer, C. L. Soles, and C. M. Stafford, Anisotropic, hierarchical surface patterns via surface wrinkling of nanopatterned polymer films, *Nano Lett.* **12**, 5995 (2012).
- [32] See Supplemental Material at <http://link.aps.org/supplemental/10.1103/PhysRevE.107.035002> for further information on sample fabrication, simulation details, detailed results of all experiments and simulations, and videos of the experiments.

- [33] F. Brau, H. Vandeparre, A. Sabbah, C. Poulard, A. Boudaoud, and P. Damman, Multiple-length-scale elastic instability mimics parametric resonance of nonlinear oscillators, *Nat. Phys.* **7**, 56 (2011).
- [34] R. Lakes, *Viscoelastic Materials* (Cambridge University Press, Cambridge, 2009).
- [35] N. Boechler, G. Theocharis, and C. Daraio, Bifurcation-based acoustic switching and rectification, *Nat. Mater.* **10**, 665 (2011).